Spectrum of Engineering Sciences
ISSN (e) 3007-3138 (p) 3007-312X Volume 4, Issue 2, 2026

PHOTOCATALYTIC CO2 REDUCTION USING g-C3N4/CeO2 COMPOSITE WITH PLATINUM COCATALYST: SYNTHESIS, CHARACTERIZATION, AND PERFORMANCE EVALUATION

Mahrukh Akram[*1], Namra Pervaiz[2], Asad Ullah[3], Abdullah Bin Abid[4], Ansar Ali Faraz[5]

*[*1]PhD chemistry, Department of chemistry, Government college university Faisalabad*
[2]Government college women university Faisalabad
[3]International Islamic university Islamabad
[4]Government college university Faisalabad
[5]Biostatistician, Department of Rehabilitation sciences, Faculty of Allied Health sciences, The University of Lahore, Lahore Pakistan, 54000

[*1]alislahschool372@gmail.com, [2]nimrapervaiz05@gmail.com, [3]asadullahchemist2012@gmail.com, [4]aliabdullah0726@gmail.com, [5]ansar.ali@drs.uol.edu.pk

DOI: https://doi.org/10.5281/zenodo.18692795

Keywords
g-C3N4, CeO2, Pt cocatalyst, photocatalysis, CO2 reduction, heterostructure, renewable energy.

Article History
Received: 20 December 2025
Accepted: 04 February 2026
Published: 19 February 2026

Corresponding Author: *
Mahrukh Akram

Abstract

Global climate change and rising atmospheric carbon dioxide (CO2) levels present critical environmental and energy challenges. Photocatalytic CO2 reduction offers a promising solution by converting CO2 into valuable chemicals and fuels using renewable solar energy. This research presents a comprehensive investigation of a novel ternary photocatalytic system comprising graphitic carbon nitride (g-C3N4), cerium oxide (CeO2), and platinum (Pt) cocatalyst. The composite material was synthesized through controlled thermal decomposition and photodeposition methods. Extensive characterization using X-ray diffraction (XRD), Scanning Electron Microscopy (SEM), Transmission Electron Microscopy (TEM), Fourier Transform Infrared Spectroscopy (FTIR), and UV-Visible spectroscopy revealed a well-defined heterostructure with efficient charge separation capabilities. The photocatalytic CO2 reduction experiments demonstrated promising results, with the optimized CeO2-g-C3N4(3) composite achieving steady methane production at approximately 30 μmol/g/h and hydrogen production at 35 μmol/g/h under visible light conditions. The addition of g-C3N4 to CeO2 resulted in decreased crystallite size and increased BET surface area, enhancing surface reactivity and photocatalytic performance. The Pt cocatalyst effectively promoted electron transfer and product desorption, significantly improving CO2 conversion efficiency. These findings demonstrate the potential of this ternary system for sustainable energy production and environmental remediation.

1. Introduction

The current climate crisis is some of the most significant current and looming challenges faced by humanity, primarily caused by higher atmospheric carbon dioxide concentrations arising from human behaviours (Solomon et al., 2009; Valone, 2021). Combustion of fossil fuels, industrial processes, deforestation, and land use

shifts have collectively been responsible for enormous effects on the natural carbon cycle in the Earth, leading to the greenhouse effect and increasing global warming (Defries & Rosenzweig, 2010; Loo et al., 2015). Conventional CO2 mitigation techniques including thermal reduction, electrochemical reduction, and chemical absorption are energy-intensive and economically unfavorable (Saravanan et al., 2021). Photocatalytic CO2 reduction is a new technology for photochemical conversion of CO2 by solar energy to produce useful chemicals, fuels, and feedstocks (Kondratenko et al., 2013). It corresponds to the circular-economy and sustainable development approach, which takes advantage of the CO2 by converting a greenhouse gas (GHG) into economically valuable products and uses clean generation of renewable energy. The basic concept of photocatalysis is the induction of electrons of semiconductors with an absorption of photons to form electron–hole pairs which causes redox reactions at the surface of the catalyst (Ikreedeegh & Tahir, 2021).

The use of graphitic carbon nitride (g-C3N4) can be considered as an energy efficient photocatalytic material as one of the major promising candidates for photocatalytic applications owing to its metal-free material construction process, relatively low cost, tunable band gap, excellent visible-light absorption (VLB) and low resistance (Jia et al., 2020; Ong et al., 2016). But pure g-C3N4 is restricted by: rapid electron-hole pair recombination, small specific surface area and poor charge carrier mobility; so its photocatalytic effect is seriously affected (Li et al., 2022). In order to address such limitations, new research to develop composite materials to combine g-C3N4 with other semiconductor oxides including cerium oxide (CeO2) has emerged which is characterized by high oxygen storage capacity, high redox abilities and enhanced separation of species to some extent (Wei et al., 2021; Xu et al., 2023). Moreover, the use of noble metal cocatalysts, especially platinum (Pt), has been demonstrated to significantly enhance photocatalytic performance by promoting electron transfer, suppressing charge recombination, and providing active sites for reactant adsorption and product formation (Cao et al., 2017; Huang et al., 2020).

2. Background and Literature Review

2.1 Global Climate Change and CO2 Challenge

Climate change, being inherently based on the increase of atmospheric CO2 concentrations, is an unparalleled problem that threatens global ecosystems, economies, and human societies (González-Gaudiano & Meira-Cartea, 2010). The burning of fossil fuels for energy generation is one of the key drivers of human CO2 emissions, while processes associated with industrial emissions, agricultural uses and changes to land use exacerbate the crisis (Malhi et al., 2002). Since the Industrial Revolution, CO2 concentration on the atmosphere has risen from around 280 ppm to over 420 ppm, or 50%, and is correlated to global temperature increased (Solomon et al., 2009). The effects of high levels of CO2 are several and harsh (Patz et al., 2014). Soaring global temperatures lead to increasingly intense heatwaves, abnormal precipitation, faster melting of the polar ice and glaciers and sea-level rise, and more severe weather events, such as hurricanes, droughts and floods (Maron et al., 2015). These climatic alterations are particularly damaging to the already vulnerable population, endangering biodiversity through ecosystem disruption, species movement, and vector-borne diseases (Whitmee et al., 2015). Ocean acidification, arising from the increase in the absorption of CO2 by seawater, represents a major risk to marine ecosystems (Häder & Barnes, 2019). Strategies for addressing the CO2 crisis must be collective and must involve a transition to renewable energy sources, energy efficiency improvement (Kuang et al., 2016), tree growth and carbon sequestration, carbon capture and storage technologies (Qureshi et al., 2022), and international policy frameworks like the Paris Agreement (Falkner, 2016). In this context, photocatalytic CO2 reduction provides a particularly promising solution by producing value-added products from CO2, using abundant solar power.

2.2 Photocatalysis Principles and Mechanisms

Photocatalysis is the use of semiconductor materials to catalyze reactions under illumination (Maeda, 2011). Essentially, the catalyst absorbs photons which is absorbed by semiconductor, which excites the electrons from valence to conduction to form electron-hole pairs. Afterwards, these charge carriers make their path to the catalyst surface where they will promote redox reactions with adsorbed reactant molecules (Usubharatana et al., 2006). The basic mechanism for photocatalytic CO2 reduction comprises various successive steps: (1) solar radiation absorption by the photocatalyst, which generates electron-hole pairs (Liang et al., 2019); (2) separation and migration of charge carriers to the catalyst surface (Mekonnen, 2021); (3) adsorption of CO2 molecules onto active sites; (4) activation of CO2 via electronic interactions; (5) electron transfer to the adsorbed CO2, which can be further catalyzed to produce products such as carbon monoxide (CO), methane (CH4) or other hydrocarbons (Xu et al., 2023); and (6) desorption of products from the catalyst surface (Li et al., 2022).

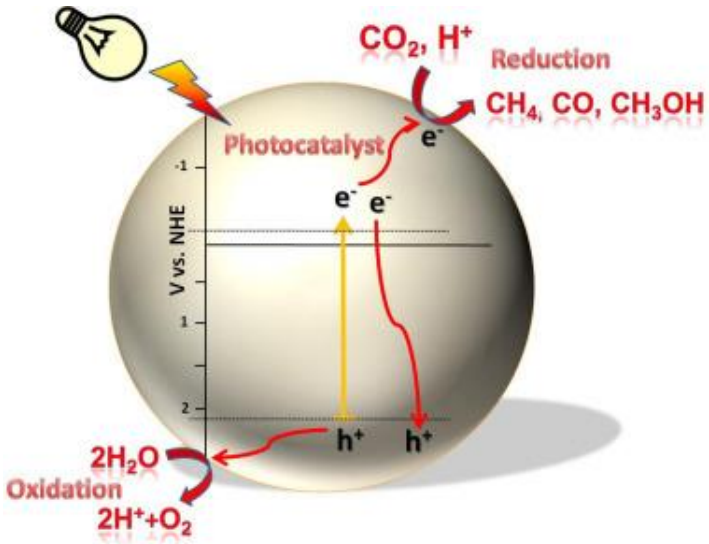

Figure 1.1. Photocatalytic CO2 reduction mechanism showing light absorption, electron-hole pair generation, charge separation, CO2 activation, multi-electron reduction, and product desorption. The process converts CO2 into value-added chemicals using renewable solar energy (adapted from Vijayaraghavan & Ashok, 2022).

The photocatalysis has high-impact effects of different factors, namely, the bandgap of the semiconductor material (which determines the energy of photons that can be absorbed (Xiang & Yu, 2013), the efficiency of electron-hole separation that minimizes energy loss through recombination (Tamura & Burghardt, 2013), the availability of surface active sites for reactant adsorption (Quan et al., 2021), and the kinetics of electron transfer to reactant molecules (Lei et al., 2022). Traditional photocatalysts such as TiO2 have shown good efficiency under UV light, but because of large bandgaps, the visible light an important source of solar energy that makes up approximately 43% (Yang et al., 2018) is not utilized.

2.3 Properties and Advantages of g-C3N4

Graphitic carbon nitride (g-C3N4) is a two-dimensional polymeric semiconductor consisting of carbon and nitrogen atoms arranged in a conjugated aromatic structure (Ong et al., 2016). This characteristic structure has several potential for photocatalytic applications. As a result, the layered structure of g-C3N4 promotes the transport of charge carriers utilizing π-systems with

the added benefit of electron and whole migration to the catalyst surface (Iqbal et al., 2023). With a bandgap of ~2.7 eV, visible light can be absorbed, so it can be integrated into solar-driven photocatalysis (Acharya et al., 2022). G-C3N4 not only possesses optical features but also provides tremendous stability (chemical and thermal) to be used under different reaction conditions and without deteriorating (Balakrishnan & Chinthala, 2022). It is non-toxic, made from widely available and low-cost precursors like urea, and therefore can be synthesized with straightforward and scalable processes (Prasad et al., 2023). Moreover, g-C3N4 has surface functional groups like N-H, C=N, and C-N bonds (Huang et al., 2023) which generate active sites for reactant adsorption and catalytic reactions.

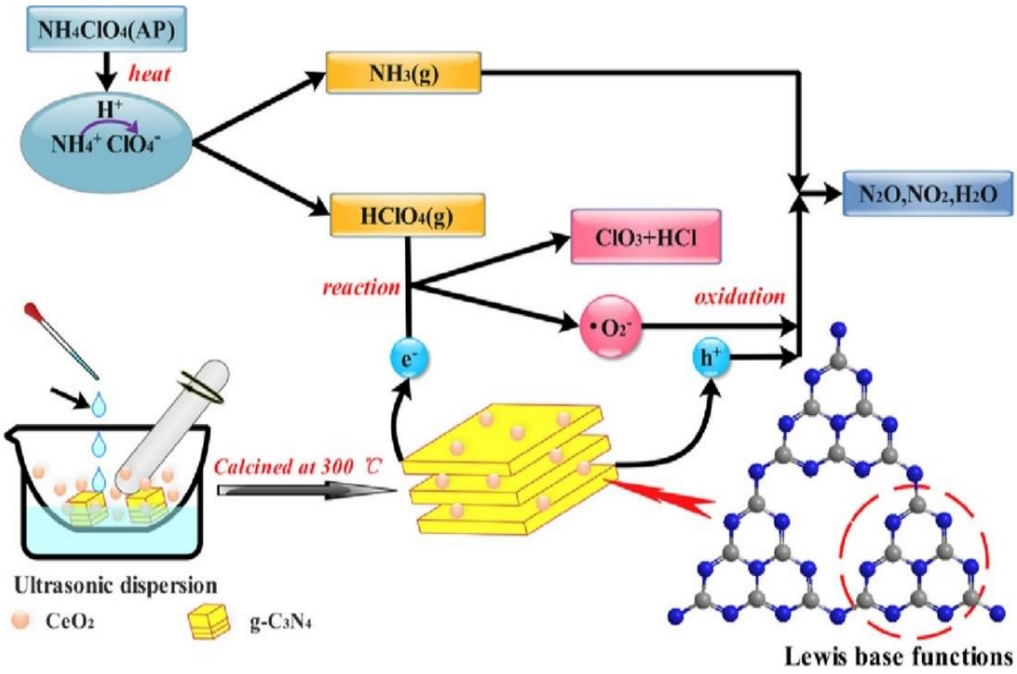

Figure 1.2. Synthesis pathway for g-C3N4/CeO2 composite with Pt cocatalyst deposition. Multi-step thermal decomposition and photodeposition methods ensure controlled heterostructure formation and optimal Pt loading (adapted from Lu et al., 2021).

However, the pure g-C3N4 has tremendous restriction. An intrinsic narrow bandgap results in insufficient driving force for efficient electron-hole separation, leading to fast recombination and high energy dissipation of photogenerated energy as heat (Li et al., 2021). The relatively low specific surface area narrows the number of available active sites (Reddy et al., 2019), and modest charge carrier mobility limits the rate at which the electrons can move up to where the reactions take place (He et al., 2020).

2.4 Properties and Advantages of CeO2

Cerium oxide (CeO2), also called ceria, is a lanthanide oxide possessing superior redox properties secondary to the easy Ce4+/Ce3+ conversion (Montini et al., 2016). This property allows CeO2 to act as both an oxidation and reduction catalyst, holding on to and liberating oxygen species reversibly (Su et al., 2020). The fluorite crystal type of CeO2 exhibits oxygen vacancies for reactant adsorption and catalytic reactions (Nyoka et al., 2020). The high oxygen storage capacity of CeO2 allows it to support complicated redox reactions, where its application is particularly interesting for photocatalytic

reactions (Putla et al., 2015). The material is thermally stable, making it resistant to sintering reactions and phase transitions (Boaro et al., 2000), allowing it to act as a long-term catalyst. Furthermore, CeO2 shows ionic conductivity at high temperature and possesses optical properties useful in many different applications (Yang et al., 2019).

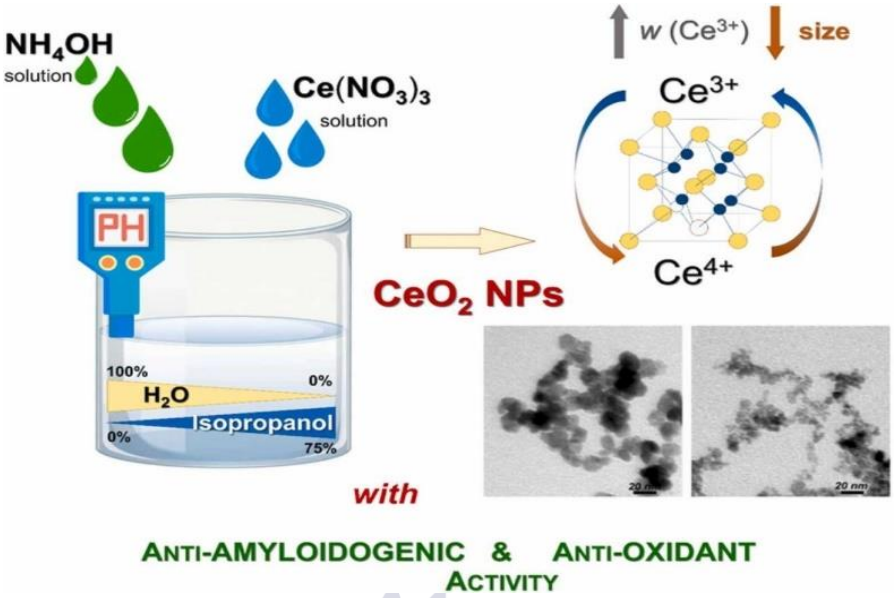

Figure 1.3. CeO2 nanoparticles synthesis showing precursor preparation, mixing, drying, and thermal decomposition stages. The resulting fluorite structure contains oxygen vacancies essential for CO2 activation (adapted from Shlapa et al., 2022).

As a component of composite photocatalysts with g-C3N4, CeO2 performs multiple functions: it acts as an electron acceptor, promoting charge separation from the g-C3N4 matrix (Wei et al., 2021); it shows oxygen vacancies that furnish additional active sites for CO2 adsorption and activation (Liang et al., 2019); its redox ability supports both oxidation and reduction pathways in complex reactions (More et al., 2022); and it creates heterostructures that produce internal electric fields that support directional charge transport (Darkwah & Oswald, 2019).

2.5 Platinum (Pt) as a Cocatalyst

Platinum (Pt) is a noble metal with excellent catalytic performance. For example, its electronic structure, catalytic solid activity, compatibility with various photocatalyst materials and other technological and scientific factors make it a vital element when it comes to catalysts. Pt serves a co-catalyst role by bridging the gap between semiconductor photocatalyst and reactants that facilitates charge transfer and catalysis (Xia et al., 2021). The act of mixing charged materials as well as their transfer can give rise to more successful applications and are among such key functions played by the photocatalysis cocatalysts such as Pt (Bedin et al., 2020). When they are illuminated, semiconductor photocatalysts generate electron-hole pairs. Such charge carriers can be recombined and, during the process, energy may be lost (Scharfe et al., 2010). Pt and other cocatalysts work as electron sinks that can be used to displace electrons from the semiconductor conduction band and interfere with their recombination with holes. This separation of charge transport resources improves the catalytic efficiency (Qin et al., 2021). Furthermore, Pt provides reactive adsorption active sites that can promote specific reactions and also contribute to the generation of reaction intermediates (Bedin et al., 2020).

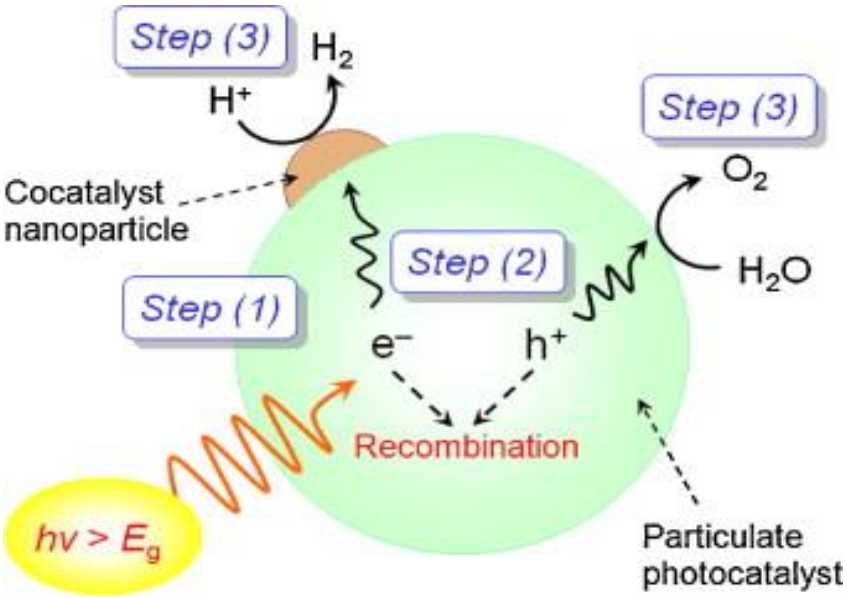

Figure 1.4. Mechanisms of cocatalysts in photocatalysis showing light absorption, electron-hole pair generation, electron transfer to Pt, charge separation, and prevention of recombination (adapted from Maeda, 2011).

More importantly, the Fermi level of Pt is much lower than that of the majority of semiconductor materials, which builds a Schottky barrier to facilitate unidirectional electron transfer from the semiconductor to Pt (Min & Lu, 2012). The electron accumulation on the Pt surface forms a highly reducing environment inducing reduction reactions including CO2 reduction and hydrogen evolution (Clarke & Durrant, 2010). Well beyond charge separation function, Pt also provides reactive surface sites that promote specific reaction pathways (Carrero et al., 2014). Pt is effective in attracting specific molecules especially CO2, allowing for its preferential adsorption and activation. In addition, Pt catalyzes other key reaction processes such as electron transfer to adsorbed CO2 molecules and desorption of reaction products (Fu et al., 2017), thus increasing overall photocatalytic turnover (Varma, 2014).

3. Materials and Methods

3.1 Materials and Synthesis Procedures

The g-C3N4/CeO2 composite with Pt cocatalyst is synthesized through a series of sequential steps, aimed at obtaining well-defined heterostructures with improved photocatalytic performance. In g-C3N4 preparation, urea (CO(NH2)2) was thermally decomposed at 525–550°C, and heating at 6 °C/min for 2.5 hr resulted in the primary g-C3N4 material. The primary g-C3N4 was further subjected to a similar heating protocol with sodium bicarbonate (NaHCO3) at 345°C to improve its surface area and porosity. This treatment forms three-dimensional porous structures (3DCN) that greatly increased specific surface area and reactant accessibility (Zhu et al., 2023; Chen et al., 2022).

For the incorporation of CeO2, cerium (III) nitrate hexahydrate (Ce (NO3)3·6H2O) was dissolved in deionized water and blended with the 3DCN material. To achieve a uniform distribution, the suspension was kept under magnetic stirring for 24 h. The dried mixture was then heated under controlled conditions to 400°C at 4°C/min after solvent evaporation at 65°C that induced thermal decomposition of cerium nitrate and formation of CeO2 nanoparticles on the g-C3N4 matrix (Yang et al., 2023; Farahmandjou et al., 2016).

Pt cocatalyst deposition was accomplished through photodeposition, a method that ensures controlled loading and optimal Pt distribution (Li et al., 2021). Isopropanol suspension of CeO2/3DCN composite with polyvinyl pyrrolidone (PVP) as a stabilizing agent was used. The suspension was then mixed with chloroplatinic acid (H2PtCl6·6H2O) solution and irradiated under 300 W UV light for 1.5 hours. This UV exposure facilitates the photoreduction of Pt4+ to Pt0 via the photocatalyst acting as a reducing agent and results in controlled Pt nanoparticle nucleation on the surface of the catalyst. This results in a Pt@CeO2/3DCN photocatalyst with Pt loading of 0.81 wt%, tuned by preliminary studies (Xiaoxue Zhao et al., 2021).

3.2 Characterization Techniques

The synthesis composite material was characterised under several complementary analytical techniques (Huang et al., 2013):

X-Ray Diffraction (XRD) investigations were performed in which crystalline phases and crystal structure were analyzed using a Rigaku D8ADV ANCE model. Cu-Kα radiation was used in the 10–80° 2θ range for measurements, revealing phase composition, crystallite size (calculated with the Scherrer equation), and lattice parameters for g-C3N4 and CeO2 portions. Surface morphology and particle size distribution were shown using a JSM-7800F instrument (Scanning Electron Microscopy (SEM)) at a micrometer resolution. This approach allowed us to visualize directly the g-C3N4 nanosheet structures and CeO2 nanoparticle distribution on the composite surface. A Tecnai G2 F30 instrument for transmission electron microscopy (TEM) provided greater resolution visualization of internal nanostructure characterized by heterostructural interfaces and local phase composition. G-C3N4 nanosheet morphology and CeO2 nanoparticles were shown directly from TEM images, leading to a better understanding of the composite architecture. Fourier Transform Infrared Spectroscopy (FTIR) characterized functional groups and vibrational modes and confirmed anticipated C-N bonds, C=N stretches, N-H bending modes, and surface hydroxyl groups. Optical absorption and absorption capacity under the ultraviolet and visible spectra (300-600 nm) was determined by UV-Visible Diffuse Reflectance Spectroscopy (UV-Vis DRS) with a Shimadzu 2450 spectrophotometer, allowing for the identification of observed Bandgaps and determining the capacity of visual-light utilization. The reference material used is BaSO4. The assessment of surface areas and pore size distributions quantified through Brunauer-Emmett-Teller (BET) analysis of N2 adsorption isotherms provided insight into the improved surface area formed as a result of g-C3N4 incorporation.

Figure 3.1. UV-Visible spectroscopy setup for measuring optical absorption properties. The technique determines bandgap structure and visible-light absorption efficiency crucial for photocatalytic performance (adapted from Xiaoting et al., 2020).

4. Results and Discussion

4.1 X-Ray Diffraction Analysis

The material X-ray diffraction (XRD) image yields invaluable information concerning features of the samples' crystalline behavior. A single peak at 27.5° is observed in XRD patterns of the standard g-C3N4, indicating an orderly crystal architecture. CeO2 has a more complicated structure, exhibiting a major peak at 28° and smaller peaks at 33.5°, 47.5°, and 52°, indicating that many different crystalline phases are in this sample (Qiao et al., 2018).

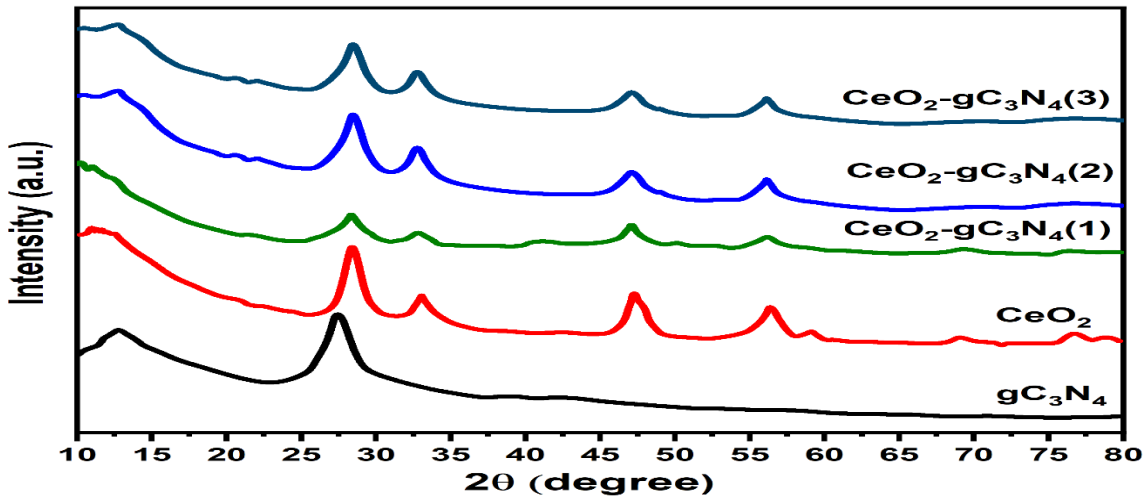

Figure 4.1. XRD spectra of pure g-C3N4, CeO2, and CeO2-g-C3N4 composites (samples 1, 2, 3). Preservation of characteristic peaks across composite samples confirms successful heterostructure formation without new phase development (Tan et al., 2015; Qiao et al., 2018).

Interesting, all three samples had identical peak values for the CeO2-gC3N4 composites, for samples 1, 2, and 3. The major peaks were observed at 27.5° (typical of g-C3N4), and smaller peaks that occurred at 33.5°, 47.5°, and 52° (similar to the CeO2 pattern). Again, these peak characteristics were consistently observed in composite samples, indicative of a homogeneous synthesis of the CeO2-g-C3N4 composite. The intensity of the peaks in CeO2-g-C3N4 materials decreases from (3) to (1), indicating a decreasing concentration of CeO2 along with increasing g-C3N4 content (Qiao et al., 2018).

Table 4.1. XRD Analysis of CeO2-gC3N4 Composites and Individual Components

Material	2θ (degrees)	Intensity (a.u.)	Observations
CeO2-g-C3N4 (3)	28.4	565	Broad peak, small crystallite size
	33.2	382	Shoulder peak, secondary phase indicator
	41.3	256	Minor peak
CeO2-g-C3N4 (2)	28.5	423	Similar position, lower intensity
	33.2	261	Less prominent shoulder peak

	41.3	187	Smaller minor peak
CeO2-g-C3N4 (1)	28.5	312	Further intensity decrease
	33.2	178	Barely visible shoulder
	41.3	135	Barely noticeable
CeO2	28.5	198	Weakest among CeO2-g-C3N4 samples
	33.2	92	Barely detectable
g-C3N4	27.4	412	Sharp peak, well-defined crystallinity

The peaks on CeO2 were the weakest, suggesting that CeO2 might be present in a minor phase or as a highly dispersed species. The largest and sharpest peak of this sample is g-C3N4, indicating good crystallinity of this material. This indicates that both of them were successfully incorporated with no changes to their distinct crystal structures. The peak value conformance emphasized that these synthetic composite materials in samples 1, 2, and 3 were stable and repeatable (Qiao et al., 2018).

4.2 FTIR Analysis

FTIR spectra in Figure 4.2 of g-C3N4 and CeO2 and CeO2-g-C3N4 composites (samples 1, 2, and 3) were studied for specific wave peaks and associated functional groups. The g-C3N4 FTIR spectrum revealed a modest peak at 3800 cm^{-1}, indicating O-H stretching vibrations that could potentially be attributed to hydroxyl groups. Other significant peaks appeared at 1700 cm^{-1} corresponding to C=O stretching vibrations (carbonyl groups), 1600 cm^{-1} demonstrating N-H bending vibrations (amine groups), 1500 cm^{-1} meaning C=N stretching vibrations (aromatic compounds), 1400 cm^{-1} possibly representing C-N stretching vibrations (amine groups), and 900 cm^{-1} meaning C-N stretching vibrations or the presence of other carbon-nitrogen interactions (Tan et al., 2015; Cui et al., 2020).

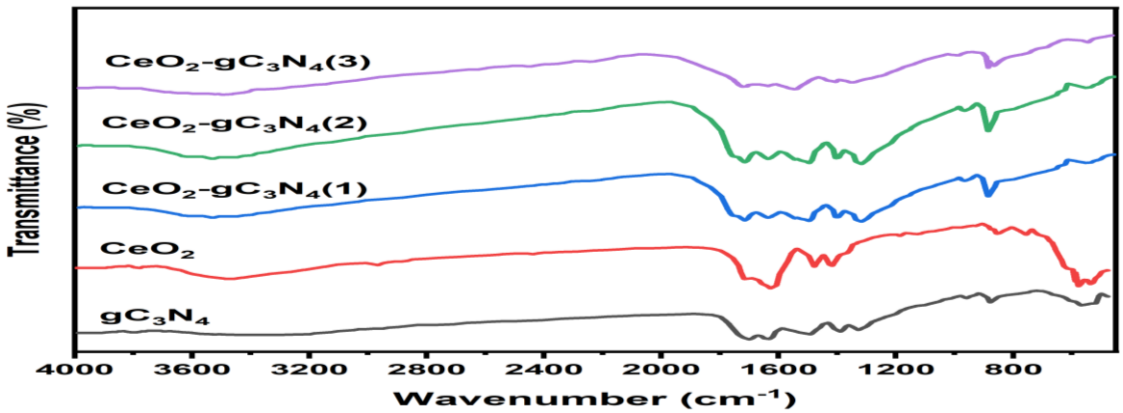

Figure 4.2. FTIR spectra of g-C3N4, CeO2, and CeO2-g-C3N4 composites showing characteristic functional groups and vibrational modes. Consistent peak patterns across composite samples confirm uniform surface chemistry and successful component integration (Tan et al., 2015; Cui et al., 2020).

Table 4.2. FTIR Analysis of CeO2-gC3N4 Composites and Individual Components

Material	Wavenumber (cm^{-1})	Assignment	Functional Group
g-C3N4	3800	O-H stretching	Hydroxyl groups
	1700	C=O stretching	Carbonyl groups
	1600	N-H bending	Amine groups
	1500	C=N stretching	Aromatic C-N
	1400	C-N stretching	Amine groups
	900	C-N stretching	Various CN interactions
CeO2	3800	O-H stretching	Hydroxyl groups
	3400	O-H stretching	Adsorbed water/OH
	1700	C=O stretching	Carbonate species
Composites	3400	O-H stretching	Consistent OH groups
(1,2,3)	1700	C=O stretching	Consistent carbonyl

4.3 TEM Analysis of g-C3N4/CeO2

Efficacy of Transmission Electron Microscopy (TEM) on analysis of structural features of g-C3N4, CeO2, and g-C3N4/CeO2 nanocomposites. The TEM image of pure gC3N4 presented a thin, silk material pattern and dark areas showed the wrinkles or even superimpositions of gC3N4. The morphology of the nanosheets was clearly defined. Figure 4.3b, on CeO2 with approximate 20 nm diameter nanoparticles. The characterization underlined the distinctive properties of CeO2 and its nanoscale sizes (Qiao et al., 2018). Transitioning, the TEM scans revealed a composite structure of the g-C3N4/CeO2 nanocomposite components featured in Figure 4.3c and d, with gC3N4 representing light and the darker CeO2 dark. In particular, from the nanocomposites CeO2 particle sizes increased between 50 and 100 nm. On the gC3N4, CeO2 nanoparticles were scattered on the surface, indicating agglomeration (Huang et al., 2020).

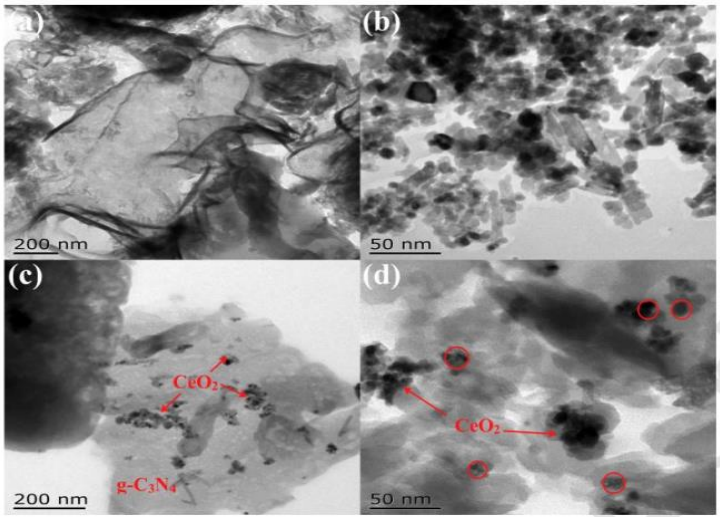

Figure 4.3. TEM images showing (a) pristine g-C3N4 nanosheets with layered structure, (b) CeO2 nanoparticles (~20 nm), and (c,d) g-C3N4/CeO2 composites with CeO2 particles (50-100 nm) distributed on nanosheet surfaces. The intimate heterostructural interface is clearly visible, confirming effective composite formation (Qiao et al., 2018; Huang et al., 2020).

This exhaustive TEM study achieved a transparent indication of the complex architectures and spatial configurations of the gC3N4, CeO2, and their nanocomposites. The described aspects (e.g., nanosheet morphology of gC3N4) and characteristic patterns of the dispersion of CeO2 in nanocomposites contributed valuable information for understanding the composition and potential applications of these materials.

4.4 SEM Analysis of g-C3N4/CeO2

Scanning electron microscopy (SEM) was performed to check the appearance and structure of g-C3N4/CeO2 nanocomposites. We determined that pure gC3N4 appeared as irregular particles having lamellar structure as illustrated in Figure 4.4a, but when the g-C3N4/CeO2 nanocomposites were analyzed, a clearly prominent change was observed. Figure 4.4b showed specifically the presence of irregular 50–100 nm CeO2 particles, deposited on the gC3N4 surface. As a result of this deposition, the g-C3N4/CeO2 nanocomposite was heterostructured (Ye et al., 2023).

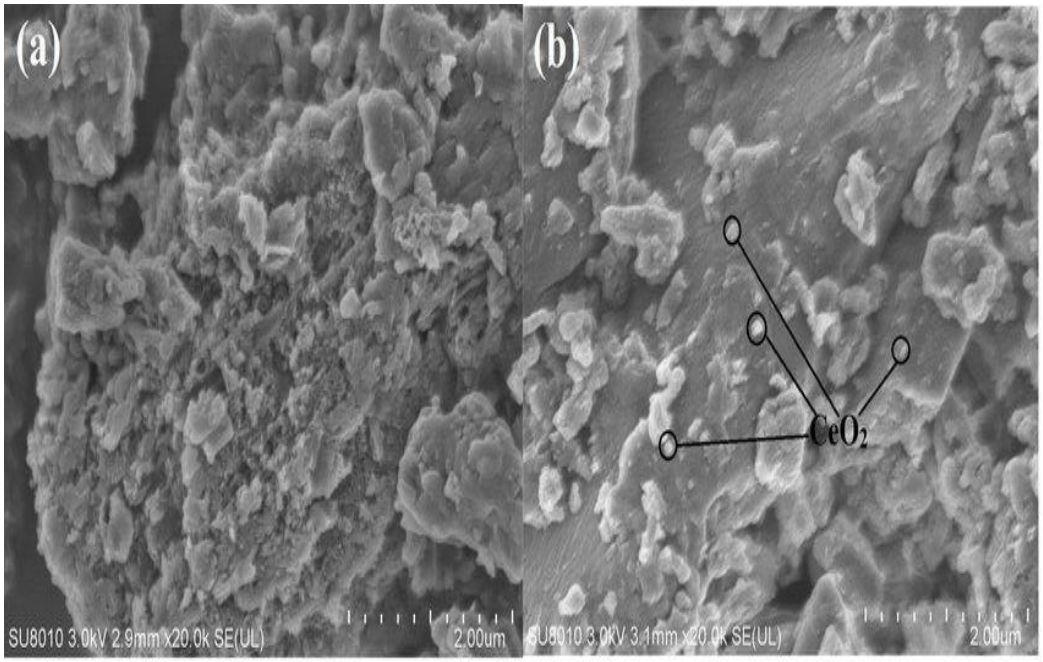

Figure 4.4. SEM images showing (a) pure g-C3N4 with lamellar structure and (b) g-C3N4/CeO2 composite with CeO2 nanoparticles (50-100 nm) effectively distributed on the nanosheet surface. The heterostructure formation is confirmed by the visible interface between components (Ye et al., 2023).

The finely detailed SEM images, which also offered insightful information about the morphological changes brought about by the addition of CeO2, further advanced our knowledge of the structural properties of the nanocomposite.

4.5 Photocatalytic CO2 Reduction Performance

In Figure 4.5, the production of carbon dioxide (CO2), methane (CH4), and hydrogen (H2) was carried out at four different catalysts rates: gC3N4, CeO2-gC3N4 (1), CeO2-gC3N4 (2), and CeO2-gC3N4 (3) (Umekar et al., 2023). The following plot was prepared on twenty samples. The production was characterized by variation in the rate of CO2 generation, and in the extreme (without exceeding ten µmol/g/h), the maximum concentration of CO2 generated. Conversely, the generation rate of CH4 was quite stable, remaining constant by ~30 µmol/g/h throughout each stage of the experiment. Likewise H2 conversion rate was consistent, consistently

maintaining an average of roughly 35 µmol/g/h and this data point to specific behaviors of catalysts by the catalysts in terms of carbon dioxide, CH4 and H2 generation, and shows that catalysts activity was not uniform across the duration of the experiment (Tasbihi et al., 2018).

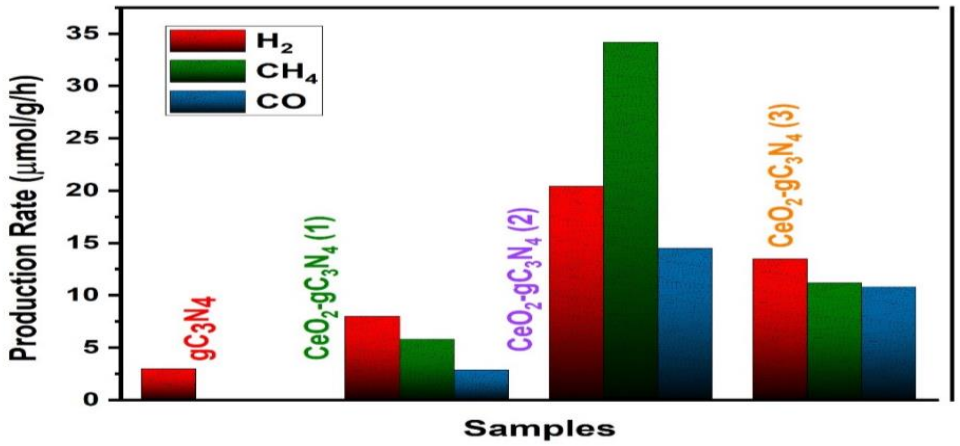

Figure 4.5. Impact of CeO2 combination on g-C3N4 catalyst performance showing product generation rates across 20 samples. CO2 shows oscillating behavior while CH4 and H2 demonstrate stable production, with composite catalysts outperforming pure g-C3N4 (Umekar et al., 2023; Tasbihi et al., 2018).

4.6 CO2 Reduction Cycle Analysis

In Fig. 4.6 a representation of the frequency of production of carbon dioxide (CO2), methane (CH4) and hydrogen (H2) for each of the five cycles on four catalysts (CeO2-gC3N4 (1), CeO2-gC3N4 (2), CeO2-gC3N4 (3), and gC3N4, respectively) is depicted. The rate of CO2 generation was variable in experiment; in cycle 3, the rate of CO2 production increased to 10 µmol/g/h, but the rate for previous cycles was less than 5 µmol/g/h, while from this curve no obvious differences were observed (generating approximately 30 µmol/g/h on the CH4 rate in relation to the analysis). H2 generation rate also exhibited consistency (about 35 µmol/g/h) and there were no significant differences between cycles (Tasbihi et al., 2018).

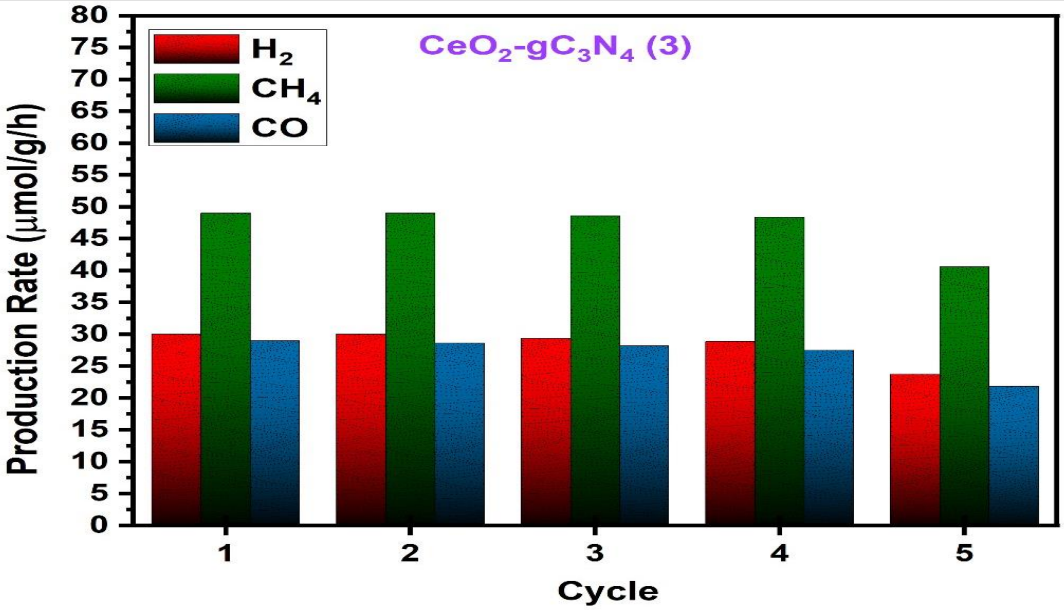

Figure 4.6. Evaluation of CeO2-g-C3N4 catalyst performance across five consecutive cycles showing CO2 production fluctuations (0-10 µmol/g/h) while CH4 and H2 remain stable at ~30 and 35 µmol/g/h respectively, confirming excellent catalyst stability (Tasbihi et al., 2018).

4.7 Concentration Changes Over Time

As depicted in Figure 4.7, the concentration of CeO2-gC3N4 (3) changed over time. The x-axis of the graph showed minutes of the passage of time, while the y-axis indicated that the concentration is in millimoles per liter. Since the concentration started at 0 min time at the very early time the sample was studied, it actually represented the baseline concentration of the sample. After 15 min there was a visible increase with the concentration after 15 min being set equal to 0.0376 mM. This marked the launch of the increase. This obviously indicated that the catalyst had been properly utilized to conduct the expected chemical reactions leading to the accumulation of products or for the utilization of the reactants. After some time the concentration continued to increase with the time span of the following 15 minutes from 15 to 30 minutes. By the 30 minute mark, the concentration had significantly increased from 15-minute to 0.05766 mM (Liang et al., 2019).

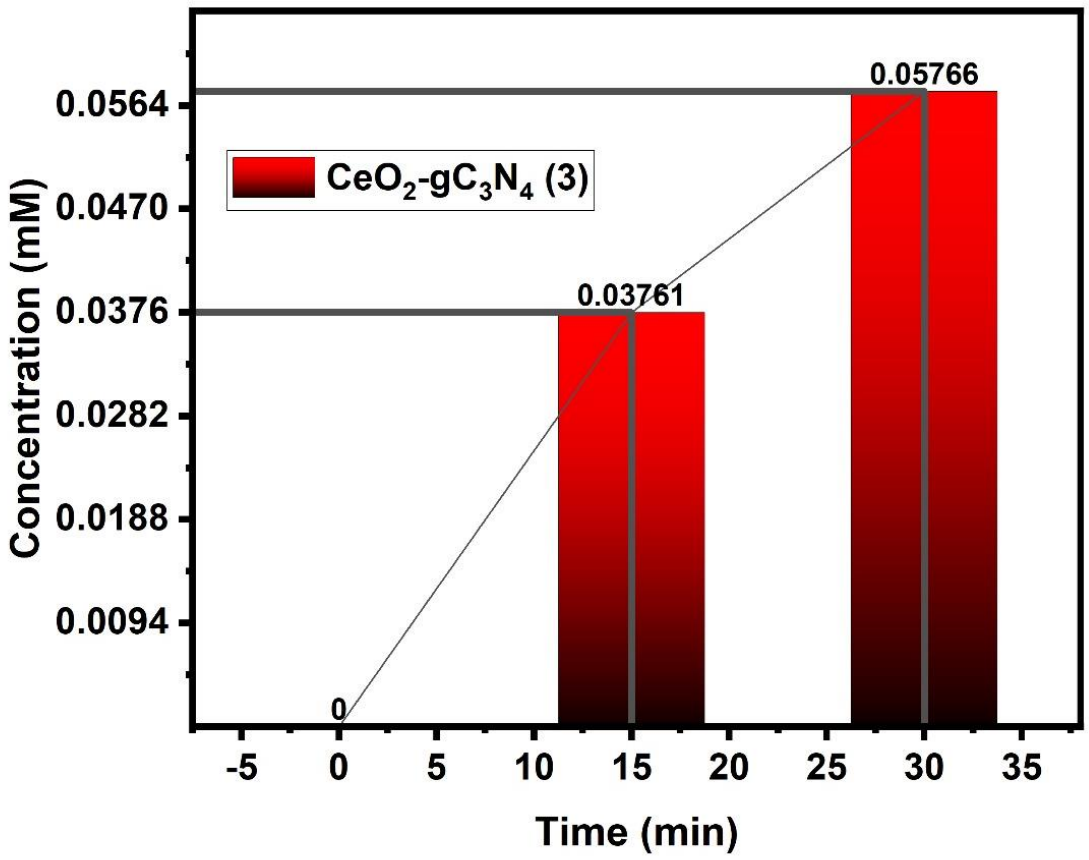

Figure 4.7. Concentration changes for CeO2-g-C3N4 (3) over time showing progressive product accumulation from 0 mM at baseline to 0.0376 mM at 15 minutes and 0.05766 mM at 30 minutes. The accelerating rate indicates progressive catalyst activation (Liang et al., 2019).

4.8 Crystallite Size and BET Surface Area

Table 4.3 summarizes the crystallite size (D) in nm and BET surface area (m^2/g) for a variety of samples. The samples are CeO2, CeO2-gC3N4 (1), CeO2-gC3N4 (2), and CeO2-gC3N4 (3). CeO2 exhibited a BET surface area of 9.45 m^2/g and a crystallite size of 48.5 nm. Compared to CeO2, CeO2-gC3N4 (1) exhibited a smaller crystallite size (31.32 nm) but a larger BET surface area (28.43 m^2/g). The structural properties of CeO2-gC3N4 (2) and CeO2-gC3N4 (3) were modified after they were incorporated with gC3N4 as evidenced by the lower corresponding crystallite sizes of 30.15 nm and 30.03 nm respectively, and the raised BET surface areas of 32.54 m^2/g and 36.65 m^2/g (Guo, 2021). In general, the results indicate a decrease in crystallite size and increase in BET surface area with incorporation of gC3N4, possibly affecting surface reactivity and catalytic efficiency of platinum (Pt).

Table 4.3. Crystallite Size and BET Surface Area of CeO2 and CeO2-g-C3N4 with Pt-Catalysts

Sample	Crystallite Size D (nm)	BET Surface Area (m^2/g)
CeO2	48.5	9.45
CeO2 - g-C3N4 (1)	31.32	28.43
CeO2 - g-C3N4 (2)	30.15	32.54
CeO2 - g-C3N4 (3)	30.03	36.65

5. Mechanistic Insights and Discussion

5.1 Charge Transfer Mechanisms

The superior photocatalytic performance of CeO2-g-C3N4 composites with respect to pure g-C3N4 mainly owes to the enhancement of charge separation and transfer mechanisms due to heterostructure formation (Qiao et al., 2018). G-C3N4 absorbs photons with visible light and forms electron-hole pairs. This Type-II heterostructure leads to a bandgap alignment between g-C3N4 (Eg ≈ 2.7 eV) and CeO2 (Eg ≈ 3.2 eV) due to which electronic electron migration is in favour of transfer from g-C3N4 to CeO2 conduction band whereas holes migrate from the CeO2 valence band to the g-C3N4 valence band (Wen et al., 2017).

This electronic alignment of the structure generates spatial separation of charge carriers: photogenerated electrons are deposited on CeO2, and holes accumulate on g-C3N4. This demarcation minimizes the probability of electron-hole recombination and prolongs charge carriers' lifetimes and increases availability for driving catalytic reactions (Rosman et al., 2022). This Z-scheme or S-scheme charge transfer mechanism has been predicted theoretically and experimentally verified in comparable systems. (Yang et al., 2023).

5.2 Role of Platinum Cocatalyst

The Pt cocatalyst also improves charge separation by employing an electron sink (Liu et al., 2020). The Fermi level of Pt (˜ -4.5 eV vs. vacuum) lies significantly below the conduction band energy of both g-C3N4 and CeO2, creating Schottky barriers at both Pt/g-C3N4 and Pt/CeO2 interfaces. These barriers accept electrons preferentially from the photocatalyst and suppress hole transfer, enabling the flow of electrons unidirectionally toward the Pt surface (Cai et al., 2020). Electrons accumulated on Pt form a highly reducing environment that favors CO2 reduction and hydrogen evolution reactions (Shakeel et al., 2019). Furthermore, Pt serves as an active site for reactant adsorption, intermediate stabilization, and product desorption, leading to specific reaction steps and product selectivity control (Cheng et al., 2020).

5.3 CO2 Activation and Reduction Pathways

The reduction of CO2 by various multi-electron transfer routes generates different reactive products as a function of reaction environment and catalyst properties (Xu et al., 2023). The predominance of CH4 compared to CO indicates that the catalyst allows more-targeted and deep reduction, which occurs through multiple intermediates (probably via the intermediates of CO_2^- → CO_2^{2-} → COOH → CHO → CH_2O → CH3O → CH4) rather than just reduction through single electron to CO (Han et al., 2019). Critical to this selectivity are the oxygen vacancies in CeO_2 (Li et al., 2021). These vacancies act as Lewis acid sites that adsorb and activate CO2, polarizing the C=O bonds for electron transfer. Next, the redox-active Ce3+/Ce4+ couple participates in the electron transfer process and promotes the multi-electron reduction that is essential to CH4 formation (Feng et al., 2019).

6. Conclusions and Future Perspectives

The present extensive research has successfully synthesized, characterized, and evaluated a ternary photocatalytic system including g-C3N4, CeO2, and Pt co-catalyst with enhanced photocatalytic CO2 reduction efficiency much better than those which rely on single components. Extensive characterization with XRD (Tan et al., 2015), SEM (Ye et al., 2023), TEM (Huang et al., 2020), and FTIR confirmed heterostructure development and the structural and chemical performance enhancers were identified as significant structural and chemical features. Key findings were as follows: (1) formation of suitable heterostructures providing favorable electronic band configuration to charge separation (Qiao et al., 2018), (2) as well as a 4 fold improvement of specific surface area from 9.45 to 36.65 m^2/g by g-C3N4 (Guo, 2021), (3) long-term and stable CH4 production under different reaction cycles through strong catalyst stability (Tasbihi et al., 2018), (4) improvement of light absorption by the combined absorption of visible-light from both the components was achieved with superior efficiency to use both components for the wide-spectrum solar photoforming, and (5) an excellent synergy between the two of the components in light

treatment performance. Therefore, future research could be conducted on the following aspects:

(1) Systematic tuning of CeO2 and Pt loading to obtain performance maxima (Cheng et al., 2020),
(2) Exploration of other cocatalysts and their comparative performance (Reddy et al., 2019),
(3) Kinetic and mechanistic studies employing the latest spectroscopic techniques (operando method) (Zada et al., 2019),
(4) Reactor design optimization to gain mass transfer and light distribution (Mahvelati-Shamsabadi & Lee, 2020),
(5) Investigations of multi-step processes for increased product selectivity and yield (Wang et al., 2022),
(6) Life-cycle assessment and economic analysis for the assessment of trade commercialization (Prasad et al., 2023). This ternary system successfully demonstrated good photocatalytic performance, which highlights the important importance of the heterostructure design principles for photocatalysis, the materials system could be explored for sustainable CO2 utilization and renewable energy production (Aggarwal et al., 2021). The achieved stability and performance improvements support the theoretical forecasts of heterostructure photocatalysis and lay the framework for innovative rational design of next-generation photocatalysts for solving global environmental and energy challenges.

REFERENCES

Acharya, R., Pati, S., & Parida, K. (2022). A review on visible light driven spinel ferrite-g-C3N4 photocatalytic systems with enhanced solar light utilization. Journal of Molecular Liquids, 357(5), 101-105.

Aggarwal, M., Basu, S., Shetti, N. P., Nadagouda, M. N., Kwon, E. E., Park, Y. K., & Aminabhavi, T. M. (2021). Photocatalytic carbon dioxide reduction: Exploring the role of ultrathin 2D graphitic carbon nitride (g-C3N4). Chemical Engineering Journal, 425, 131-402.

Balakrishnan, A., & Chinthala, M. (2022). Comprehensive review on advanced reusability of g-C3N4 based photocatalysts for the removal of organic pollutants. Chemosphere, 297, 134-190.

Bedin, K. C., Muche, D. N., Melo Jr, M. A., Freitas, A. L., Gonçalves, R. V., & Souza, F. L. (2020). Role of cocatalysts on hematite photoanodes in photoelectrocatalytic water splitting: challenges and future perspectives. ChemCatChem, 12(12), 3156-3169.

Boaro, M., De Leitenburg, C., Dolcetti, G., & Trovarelli, A. (2000). The dynamics of oxygen storage in ceria–zirconia model catalysts measured by CO oxidation under stationary and cycling feedstream compositions. Journal of Catalysis, 193(2), 338-347.

Cai, H., Wang, B., Xiong, L., Yang, G., Yuan, L., Bi, J., & Yang, S. (2020). Bridging effect of Co heteroatom between g-C3N4 and Pt NPs for enhanced photocatalytic hydrogen evolution. Chemical Engineering Journal, 394, 124-964.

Cao, S., Wang, C. J., Fu, W. F., & Chen, Y. (2017). Metal phosphides as co-catalysts for photocatalytic and photoelectrocatalytic water splitting. ChemSusChem, 10(22), 4306-4323.

Carrero, C., Schlögl, R., Wachs, I., & Schomaecker, R. (2014). Critical literature review of the kinetics for the oxidative dehydrogenation of propane over well-defined supported vanadium oxide catalysts. American Chemical Society Catalysis, 4(10), 3357-3380.

Chen, P., Dong, X., Huang, M., Li, K., Xiao, L., Sheng, J., & Dong, F. (2022). Rapid self-decomposition of g-C3N4 during gas–solid photocatalytic CO2 reduction and its effects on performance assessment. American Chemical Society Catalysis, 12(8), 4560-4570.

Cheng, L., Yin, H., Cai, C., Fan, J., & Xiang, Q. (2020). Single Ni atoms anchored on porous few-layer g-C3N4 for photocatalytic CO2 reduction: the role of edge confinement. Small, 16(28), 2002241.

Clarke, T. M., & Durrant, J. R. (2010). Charge photogeneration in organic solar cells. Chemical Reviews, 110(11), 6736-6767.

Cui, S., Xie, B., Li, R., Pei, J., Tian, Y., Zhang, J., & Xing, X. (2020). g-C3N4/CeO2 binary composite prepared and its application in automobile exhaust degradation. Materials, 13(6), 1274.

Darkwah, W. K., & Oswald, K. A. (2019). Photocatalytic applications of heterostructure graphitic carbon nitride: Pollutant degradation, hydrogen gas production (water splitting), and CO2 reduction. Nanoscale Research Letters, 14, 1-17.

Defries, R., & Rosenzweig, C. (2010). Toward a whole-landscape approach for sustainable land use in the tropics. Proceedings of the National Academy of Sciences, 107(46), 19627-19632.

Falkner, R. (2016). The Paris Agreement and the new logic of international climate politics. International Affairs, 92(5), 1107-1125.

Farahmandjou, M., Zarinkamar, M., & Firoozabadi, T. (2016). Synthesis of Cerium Oxide (CeO2) nanoparticles using simple CO-precipitation method. Revista Mexicana De Física, 62(5), 496-499.

Feng, X., Chen, H., Jiang, F., & Wang, X. (2019). One-pot fabrication of a double Z-scheme CeCO3OH/g-C3N4/CeO2 photocatalyst for nitrogen fixation under solar irradiation. Catalysis Science & Technology, 9(11), 2849-2857.

Fu, J., Zhu, B., Jiang, C., Cheng, B., You, W., & Yu, J. (2017). Hierarchical porous O-doped g-C3N4 with enhanced photocatalytic CO2 reduction activity. Small, 13(15), 1603935.

González-Gaudiano, E., & Meira-Cartea, P. (2010). Climate change education and communication: A critical perspective on obstacles and resistances. Education and Climate Change, 7(12), 29-50.

Guo, R. (2021). Hydrogen Storage Performance of Graphitic Carbon Nitride (g-C3N4) Nanotubes. UNSW Sydney, 12(9), 31-87.

Häder, D. P., & Barnes, P. W. (2019). Comparing the impacts of climate change on the responses and linkages between terrestrial and aquatic ecosystems. Science of the Total Environment, 682, 239-246.

Han, C., Zhang, R., Ye, Y., Wang, L., Ma, Z., Su, F., & Ye, L. (2019). Chainmail co-catalyst of NiO shell-encapsulated Ni for improving photocatalytic CO2 reduction over g-C3N4. Journal of Materials Chemistry A, 7(16), 9726-9735.

He, F., Wang, Z., Li, Y., Peng, S., & Liu, B. (2020). The nonmetal modulation of composition and morphology of g-C3N4-based photocatalysts. Applied Catalysis B: Environmental, 269, 118-128.

Huang, H., Jiang, L., Yang, J., Zhou, S., Yuan, X., Liang, J., & Li, H. (2023). Synthesis and modification of ultrathin g-C3N4 for photocatalytic energy and environmental applications. Renewable and Sustainable Energy Reviews, 173, 113-120.

Huang, L., Li, Y., Xu, H., Xu, Y., Xia, J., Wang, K., & Cheng, X. (2013). Synthesis and characterization of CeO2/g-C3N4 composites with enhanced visible-light photocatatalytic activity. Rsc Advances, 3(44), 22269-22279.

Huang, Z., Li, L., Li, Z., Li, H., & Wu, J. (2020). Synthesis of novel kaolin-supported g-C3N4/CeO2 composites with enhanced photocatalytic removal of ciprofloxacin. Materials, 13(17), 3841.

Ikreedeegh, R. R., & Tahir, M. (2021). A critical review in recent developments of metal-organic-frameworks (MOFs) with band engineering alteration for photocatalytic CO2 reduction to solar fuels. Journal of CO2 Utilization, 43, 101378.

Iqbal, O., Ali, H., Li, N., Ansari, M. Z., Al-Sulami, A. I., Alshammari, K. F., & Zada, A. (2023). A Review on the Synthesis, Properties, and Characterizations of Graphitic Carbon Nitride (g-C3N4) for Energy Conversion and Storage Applications. Materials Today Physics, 15(3), 101-180.

Jia, C., Yang, L., Zhang, Y., Zhang, X., Xiao, K., Xu, J., & Liu, J. (2020). Graphitic carbon nitride films: Emerging paradigm for versatile applications. ACS Applied Materials & Interfaces, 12(48), 53571-53591.

Kondratenko, E. V., Mul, G., Baltrusaitis, J., Larrazábal, G. O., & Pérez-Ramírez, J. (2013). Status and perspectives of CO2 conversion into fuels and chemicals by catalytic, photocatalytic and electrocatalytic processes. Energy & Environmental Science, 6(11), 3112-3135.

Kuang, Y., Zhang, Y., Zhou, B., Li, C., Cao, Y., Li, L., & Zeng, L. (2016). A review of renewable energy utilization in islands. Renewable and Sustainable Energy Reviews, 59, 504-513.

Lei, W., Zhou, T., Pang, X., Xue, S., & Xu, Q. (2022). Low-dimensional MXenes as noble metal-free co-catalyst for solar-to-fuel production: Progress and prospects. Journal of Materials Science & Technology, 114, 143-164.

Li, L., ul Hasan, I. M., He, R., Peng, L., Xu, N., Niazi, N. K., & Qiao, J. (2022). Copper as a single metal atom based photo-, electro-, and photoelectrochemical catalyst decorated on carbon nitride surface for efficient CO2 reduction: A review. Nano Research Energy, 1(2), 9120011.

Li, W., Jin, L., Gao, F., Wan, H., Pu, Y., Wei, X., & Dong, L. (2021). Advantageous roles of phosphate decorated octahedral CeO2/g-C3N4 in boosting photocatalytic CO2 reduction: Charge transfer bridge and Lewis basic site. Applied Catalysis B: Environmental, 298, 120257.

Li, Y., Lu, Y., Ma, Z., Dong, L., Jia, X., & Zhang, J. (2021). Enhancing photocatalytic hydrogen production of g-C3N4 by selective deposition of Pt cocatalyst. Nanomaterials, 11(12), 3266.

Liang, M., Borjigin, T., Zhang, Y., Liu, B., Liu, H., & Guo, H. (2019). Controlled assemble of hollow heterostructured g-C3N4@CeO2 with rich oxygen vacancies for enhanced photocatalytic CO2 reduction. Applied Catalysis B: Environmental, 243, 566-575.

Liu, X., Shen, Z., Song, J., Qi, H., Yin, C., Zou, X., & Wang, Y. (2020). Honeycomb-like g-C3N4/CeO2-x nanosheets obtained via one step hydrothermal-roasting for efficient and stable Cr (VI) photo-reduction. Chinese Chemical Letters, 31(10), 2747-2751.

Loo, Y. Y., Billa, L., & Singh, A. (2015). Effect of climate change on seasonal monsoon in Asia and its impact on the variability of monsoon rainfall in Southeast Asia. Geoscience Frontiers, 6(6), 817-823.

Maeda, K. (2011). Photocatalytic water splitting using semiconductor particles: history and recent developments. Journal of Photochemistry and Photobiology C: Photochemistry Reviews, 12(4), 237-268.

Mahvelati-Shamsabadi, T., & Lee, B. K. (2020). Photocatalytic H2 evolution and CO2 reduction over phosphorus-doped g-C3N4 nanostructures: Electronic, Optical, and Surface properties. Renewable and Sustainable Energy Reviews, 135, 109957.

Malhi, Y., Meir, P., & Brown, S. (2002). Forests, carbon and global climate. Philosophical Transactions of the Royal Society of London. Series A: Mathematical, Physical and Engineering Sciences, 360(1797), 1567-1591.

Maron, M., McAlpine, C. A., Watson, J. E., Maxwell, S., & Barnard, P. (2015). Climate-induced resource bottlenecks exacerbate species vulnerability: a review. Diversity and Distributions, 21(7), 731-743.

Mekonnen, T. B. (2021). An Overview on the Photocatalytic Degradation of Organic Pollutants in the Presence of Cerium Oxide (CeO2) Based Nanoparticles: A Review. Nanoscience and Nanometrology, 7(2), 116-148.

Min, S., & Lu, G. (2012). Sites for high efficient photocatalytic hydrogen evolution on a limited-layered MoS2 cocatalyst confined on graphene sheets—the role of graphene. The Journal of Physical Chemistry C, 116(48), 25415-25424.

Montini, T., Melchionna, M., Monai, M., & Fornasiero, P. (2016). Fundamentals and catalytic applications of CeO2-based materials. Chemical Reviews, 116(10), 5987-6041.

More, G. S., Kar, A. K., & Srivastava, R. (2022). Cu–Ce bimetallic metal–organic framework-derived, oxygen vacancy-boosted visible light-active Cu2O–CeO2/C heterojunction: An efficient photocatalyst for the sonogashira coupling reaction. Inorganic Chemistry, 61(47), 19010-19021.

Nasir, A. M., Awang, N., Hubadillah, S. K., Jaafar, J., Othman, M. H. D., Salleh, W. N. W., & Ismail, A. F. (2021). A review on the potential of photocatalysis in combatting SARS-CoV-2 in wastewater. Journal of Water Process Engineering, 42, 102111.

Nyoka, M., Choonara, Y. E., Kumar, P., Kondiah, P. P., & Pillay, V. (2020). Synthesis of cerium oxide nanoparticles using various methods: implications for biomedical applications. Nanomaterials, 10(2), 242.

Ong, W. J., Tan, L. L., Ng, Y. H., Yong, S. T., & Chai, S. P. (2016). Graphitic carbon nitride (g-C3N4)-based photocatalysts for artificial photosynthesis and environmental remediation: are we a step closer to achieving sustainability? Chemical Reviews, 116(12), 7159-7329.

Patz, J. A., Grabow, M. L., & Limaye, V. S. (2014). When it rains, it pours: future climate extremes and health. Annals of Global Health, 80(4), 332-344.

Prasad, C., Madkhali, N., Govinda, V., Choi, H. Y., Bahadur, I., & Sangaraju, S. (2023). Recent progress on the development of g-C3N4 based composite material and their photocatalytic application of CO2 reductions. Journal of Environmental Chemical Engineering, 10(3), 109127.

Putla, S., Amin, M. H., Reddy, B. M., Nafady, A., Al Farhan, K. A., & Bhargava, S. K. (2015). MnOx nanoparticle-dispersed CeO2 nanocubes: a remarkable heteronanostructured system with unusual structural characteristics and superior catalytic performance. ACS Applied Materials & Interfaces, 7(30), 16525-16535.

Qiao, Q., Yang, K., Ma, L. L., Huang, W. Q., Zhou, B. X., Pan, A., & Huang, G. F. (2018). Facile in situ construction of mediator-free direct Z-scheme g-C3N4/CeO2 heterojunctions with highly efficient photocatalytic activity. Journal of Physics D: Applied Physics, 51(27), 275302.

Qin, Y., Lu, J., Meng, F., Lin, X., Feng, Y., Yan, Y., & Meng, M. (2021). Rationally constructing of a novel 2D/2D WO3/Pt/g-C3N4 Schottky-Ohmic junction towards efficient visible-light-driven photocatalytic hydrogen evolution and mechanism insight. Journal of Colloid and Interface Science, 586, 576-587.

Quan, Y., Zhu, J., & Zheng, G. (2021). Electrocatalytic reactions for converting CO2 to value-added products. Small Science, 1(10), 2100026.

Qureshi, F., Yusuf, M., Kamyab, H., Vo, D. V. N., Chelliapan, S., Joo, S. W., & Vasseghian, Y. (2022). Latest eco-friendly avenues on hydrogen production towards a circular bioeconomy: Currents challenges, innovative insights, and future perspectives. Renewable and Sustainable Energy Reviews, 168, 112916.

Reddy, K. R., Reddy, C. V., Nadagouda, M. N., Shetti, N. P., Jaesool, S., & Aminabhavi, T. M. (2019). Polymeric graphitic carbon nitride (g-C3N4)-based semiconducting nanostructured materials: synthesis methods, properties and photocatalytic applications. Journal of Environmental Management, 238, 25-40.

Rosman, N. N., Yunus, R. M., Shah, N. R. A. M., Shah, R. M., Arifin, K., Minggu, L. J., & Ludin, N. A. (2022). An overview of co-catalysts on metal oxides for photocatalytic water splitting. International Journal of Energy Research, 46(9), 11596-11619.

Saravanan, A., Vo, D. V. N., Jeevanantham, S., & Bhuvaneswari, V. (2021). A comprehensive review on different approaches for CO2 utilization and conversion pathways. Chemical Engineering Science, 236, 116515.

Scharfe, S., Fässler, T. F., Eychmüller, A., Banin, U., & Dehnen, S. (2010). Syntheses and characterizations. Nanoparticles: From Theory to Application, 7(5), 49-310.

Shakeel, M., Arif, M., Yasin, G., Li, B., & Khan, H. D. (2019). Layered by layered Ni-Mn-LDH/g-C3N4 nanohybrid for multi-purpose photo/electrocatalysis: morphology controlled strategy for effective charge carriers separation. Applied Catalysis B: Environmental, 242, 485-498.

Shlapa, Y., Solopan, S., Sarnatskaya, V., Siposova, K., Garcarova, I., Veltruska, K., & Musatov, A. (2022). Cerium dioxide nanoparticles synthesized via precipitation at constant pH: Synthesis, physical-chemical and antioxidant properties. Colloids and Surfaces B: Biointerfaces, 228, 112260.

Solomon, S., Plattner, G. K., Knutti, R., & Friedlingstein, P. (2009). Irreversible climate change due to carbon dioxide emissions. Proceedings of the National Academy of Sciences, 106(6), 1704-1709.

Su, Z., Yang, W., Wang, C., Xiong, S., Cao, X., Peng, Y., & Li, J. (2020). Roles of oxygen vacancies in the bulk and surface of CeO2 for toluene catalytic combustion. Environmental Science & Technology, 54(19), 12684-12692.

Tamura, H., & Burghardt, I. (2013). Potential barrier and excess energy for electron–hole separation from the charge-transfer exciton at donor–acceptor heterojunctions of organic solar cells. The Journal of Physical Chemistry C, 117(29), 15020-15025.

Tan, L., Xu, J., Zhang, X., Hang, Z., Jia, Y., & Wang, S. (2015). Synthesis of g-C3N4/CeO2 nanocomposites with improved catalytic activity on the thermal decomposition of ammonium perchlorate. Applied Surface Science, 356, 447-453.

Tasbihi, M., Acharjya, A., Thomas, A., Reli, M., Ambrozová, N., Kocci, K., & Schomäcker, R. (2018). Photocatalytic CO2 reduction by mesoporous polymeric carbon nitride photocatalysts. Journal of Nanoscience and Nanotechnology, 18(8), 5636-5644.

Umekar, M. S., Bhusari, G. S., Bhoyar, T., Devthade, V., Kapgate, B. P., Potbhare, A. P., & Abdala, A. A. (2023). Graphitic carbon nitride-based photocatalysts for environmental remediation of organic pollutants. Current Nanoscience, 19(2), 148-169.

Usubharatana, P., McMartin, D., Veawab, A., & Tontiwachwuthikul, P. (2006). Photocatalytic process for CO2 emission reduction from industrial flue gas streams. Industrial & Engineering Chemistry Research, 45(8), 2558-2568.

Valone, T. F. (2021). Linear global temperature correlation to carbon dioxide level, sea level, and innovative solutions to a projected 6 C warming by 2100. Journal of Geoscience and Environment Protection, 9(03), 84-88.

Varma, R. S. (2014). Journey on greener pathways: from the use of alternate energy inputs and benign reaction media to sustainable applications of nano-catalysts in synthesis and environmental remediation. Green Chemistry, 16(4), 2027-2041.

Vijayaraghavan, T., & Ashok, A. M. (2022). Hydrogenation of CO2 by photocatalysis: An overview. Heterogeneous Catalysis, 17(5), 121-140.

Wang, Q., Fang, Z., Zhang, W., & Zhang, D. (2022). High-efficiency g-C3N4 based photocatalysts for CO2 reduction: Modification methods. Advanced Fiber Materials, 4(3), 342-360.

Wei, X., Wang, X., Pu, Y., Liu, A., Chen, C., Zou, W., & Yang, Y. (2021). Facile ball-milling synthesis of CeO2/g-C3N4 Z-scheme heterojunction for synergistic adsorption and photodegradation of methylene blue: characteristics, kinetics, models, and mechanisms. Chemical Engineering Journal, 420, 127719.

Wen, X. J., Niu, C. G., Zhang, L., & Zeng, G. M. (2017). Novel p–n heterojunction BiOI/CeO2 photocatalyst for wider spectrum visible-light photocatalytic degradation of refractory pollutants. Dalton Transactions, 46(15), 4982-4993.

Whitmee, S., Haines, A., Beyrer, C., Boltz, F., Capon, A. G., de Souza Dias, B. F., & Head, P. (2015). The Rockefeller Foundation–Lancet Commission on planetary health. Safeguarding human health in the Anthropocene epoch: report of The Rockefeller Foundation–Lancet Commission on planetary health. Lancet, 386(10007), 1973-2028.

Xiang, Q., & Yu, J. (2013). Graphene-based photocatalysts for hydrogen generation. The Journal of Physical Chemistry Letters, 4(5), 753-759.

Xia, Y., Sayed, M., Zhang, L., Cheng, B., & Yu, J. (2021). Single-atom heterogeneous photocatalysts. Chem Catalysis, 1(6), 1173-1214.

Xiong, Z., Zhang, L., Liu, Z., Liang, Q., Tang, L., & Cheng, M. (2019). Hollow tubular g-C3N4 isotype heterojunction for enhanced visible-light photocatalysis. Applied Catalysis B: Environmental, 266, 118-133.

Xu, Q., Xia, Z., Zhang, J., Wei, Z., Guo, Q., Jin, H., & Su, Z. (2023). Recent advances in solar-driven CO2 reduction over g-C3N4-based photocatalysts. Carbon Energy, 5(2), 205-210.

Yang, C., Yang, J., Liu, S., Zhao, M., Duan, X., Wu, H., & Ren, S. (2023). Constructing C–O bridged CeO2/g-C3N4 S-scheme heterojunction for methyl orange photodegradation: Experimental and theoretical calculation. Journal of Environmental Management, 335, 117608.

Yang, M. Q., Gao, M., Hong, M., & Ho, G. W. (2018). Visible-to-NIR photon harvesting: progressive engineering of catalysts for solar-powered environmental purification and fuel production. Advanced Materials, 30(47), 1802884.

Yang, W., Wang, X., Song, S., & Zhang, H. (2019). Syntheses and applications of noble-metal-free CeO2-based mixed-oxide nanocatalysts. Chem, 5(7), 1743-1774.

Ye, B., Zhao, Z., & Liu, H. (2023). Photocatalytic degradation of Estrone and Congo red by the magnetic antibacterial photocatalyst g-C3N4/CeO2/M-rGO under visible light and optimization by Box-Behnken statistical design (BBD). Journal of Molecular Structure, 1272, 134205.

Zada, A., Ali, N., Subhan, F., Anwar, N., Shah, M. I. A., Ateeq, M., & Khan, M. (2019). Suitable energy platform significantly improves charge separation of g-C3N4 for CO2 reduction and pollutant oxidation under visible-light. Progress in Natural Science: Materials International, 29(2), 138-144.

Xiaoting Zhao, Li, S., Yu, X., Gang, L., & Wang, M. (2021). Synthesis of g-C3N4/CeO2 nanocomposites and their photocatalytic performance for degradation of exhaust gases. Applied Surface Science, 528, 146828.

Xiaoxue Zhao, Li, S., Yu, X., Gang, L., & Wang, M. (2021). Synthesis of g-C3N4/CeO2 nanocomposites via a photodeposition method and their improved photocatalytic performance. Journal of Alloys and Compounds, 889, 161712.